

# XGAP with uGMRT I: Old AGN plasma in merging galaxy groups

R. Santra<sup>1, \*</sup>, R. Kale<sup>1</sup>, K. Kolokythas<sup>2,3</sup>, M. Brienza<sup>4</sup>, E. O’Sullivan<sup>5</sup>, D. Eckert<sup>6</sup>, F. de. Gasperin<sup>4</sup>, T. Pasini<sup>4</sup>, F. Gastaldello<sup>7</sup>, A. Finoguenov<sup>8</sup>, M. Sun<sup>9</sup>, G. Gozaliasl<sup>8,10</sup>, and M. Bourne<sup>11,12</sup>

<sup>1</sup> National Centre for Radio Astrophysics, Tata Institute of Fundamental Research, S. P. Pune University, Ganeshkhind, Pune 411007, India

<sup>2</sup> Centre for Radio Astronomy Techniques and Technologies, Department of Physics and Electronics, Rhodes University, P.O. Box 94, Makhanda 6140, South Africa

<sup>3</sup> South African Radio Astronomy Observatory, Black River Park North, 2 Fir St, Cape Town, 7925, South Africa

<sup>4</sup> Istituto Nazionale di Astrofisica (INAF) - Istituto di Radioastronomia (IRA), via Gobetti 101, 40129, Bologna, Italy

<sup>5</sup> Center for Astrophysics | Harvard & Smithsonian, 60 Garden Street, Cambridge, MA 02138, USA

<sup>6</sup> Department of Astronomy, University of Geneva, Ch. d’Ecogia 16, CH-1290 Versoix, Switzerland

<sup>7</sup> INAF - IASF Milano, via A. Corti 12, 20133 Milano, Italy

<sup>8</sup> Department of Physics, University of Helsinki, P. O. Box 64, FI00014 Helsinki, Finland

<sup>9</sup> Department of Physics and Astronomy, University of Alabama in Huntsville, 301 Sparkman Drive, Huntsville, AL 35899, USA

<sup>10</sup> Department of Computer Science, Aalto University, PO Box 15400, Espoo, FI-00076, Finland

<sup>11</sup> Centre for Astrophysics Research, Department of Physics, Astronomy and Mathematics, University of Hertfordshire, College Lane, Hatfield AL10 9AB, UK

<sup>12</sup> Kavli Institute for Cosmology, University of Cambridge, Madingley Road, Cambridge CB3 0HA, UK

February 6, 2026

## ABSTRACT

**Context.** Galaxy groups are significantly affected by outflows from central Active Galactic Nuclei (AGN), especially due to the shallower gravitational potential compared to galaxy clusters. The group binding energy is comparable to the energy output from AGN, making it an important factor in mutual evolution.

**Aims.** We present a multi-wavelength analysis of three dynamically active groups—SDSSTG8102, SDSSTG16393, and SDSSTG28674—which are part of the *XMM-Newton* Group AGN Project X-GAP sample, a statistically complete sample of 49 galaxy groups, to understand the central AGN evolution.

**Methods.** We combine proprietary uGMRT 400 MHz observations, with 144 MHz LOFAR, and *XMM-Newton* observations to study the radio sources associated with the respective Brightest Group Galaxies (BGGs).

**Results.** The BGGs in SDSSTG8102 and SDSSTG16393 have extended radio emission with asymmetric distortions in their morphologies. SDSSTG28674 has a compact flat-spectrum radio source associated with the BGG and an extended lobe on one side, which is connected to it with a faint bridge detected with LOFAR. Integrated spectral indices of the three BGGs are  $-0.96 \pm 0.09$  (SDSSTG8102),  $-1.35 \pm 0.09$  (SDSSTG16393), and  $-1.6 \pm 0.02$  (SDSSTG28674). X-ray images reveal elongated morphologies in all three groups, SDSSTG28674 showing evidence of a binary merger, while thermodynamical maps highlight temperature variations.

**Conclusions.** In SDSSTG8102, lobes are bent and displaced by IGrM flows, while SDSSTG16393 hosts steep-spectrum relic-like plasma coinciding with X-ray emission. SDSSTG28674, with its ultra-steep spectrum lobe and disturbed morphology, likely traces merger-driven activity, consistent with a remnant or revived radio phoenix. The spectral diversity across the systems reflects different stages of AGN fading governed by duty cycle, source age, and confinement by the hot IGrM. The presence of bright group-scale X-ray halos ( $\sim 300$  kpc) and  $>50$  kpc radio emission, combined with disturbed morphologies, underscores the central role of IGrM confinement and merger-driven gas motions in sustaining extended diffuse structures. The multi-band radio follow-up of the entire X-GAP sample will allow further insights.

**Key words.** Galaxies: groups: general – Galaxies: interactions – large-scale structure of universe – radiation mechanism: non-thermal – methods: observational – radio continuum: general

## 1. Introduction

Galaxy groups are gravitationally bound systems that house the majority of galaxies and stars in the Universe (e.g., Eke et al. 2004; Robotham et al. 2011). These groups encompass more than half of all galaxies, compared to only about 2% found in galaxy clusters, making them the most common type of environment in the local Universe (e.g., Geller & Huchra 1983). Although galaxy groups are less massive than clusters, typically having  $M_{500} < 10^{14} M_{\odot}$ , and contain fewer members, they play

a pivotal role in the formation of large-scale structures (e.g., Grogin & Geller 2000; Lovisari et al. 2021). In the hierarchical model of structure formation, galaxy clusters are thought to form through the merging of smaller groups (e.g., van den Bosch et al. 2014; Haines et al. 2018; Nelson et al. 2024). As a result, the early evolution of galaxies in rich clusters (e.g., Beck et al. 1999) is closely connected to the processes that shape galaxies within groups. Galaxy groups should not be seen simply as the scaled-down versions of galaxy clusters (e.g., Ponman et al. 1999, 2003; Sun 2012). They are characterised by shallow gravitational potentials and low velocity dispersions, which

\* ramananda1999@gmail.com

create environments conducive to galaxy mergers and tidal interactions, in turn driving rapid galaxy evolution (e.g., McIntosh et al. 2008; Alonso et al. 2012; Solanes et al. 2018). Therefore, studying galaxy groups is essential for developing a more complete understanding of galaxy formation and evolution, as well as the mechanisms behind these processes (e.g., Forbes et al. 2006; Kolokythas et al. 2019).

Unlike virialised clusters, where the hot gas permeating the system volume (called the intracluster medium) is consistently the dominant baryonic component, group gas content varies significantly (e.g., Sun et al. 2009; Eckert et al. 2012; Lovisari et al. 2015). It is now known that the more massive and evolved galaxy groups are dominated by early-type galaxies that present little cold gas (HI) but often host an extended hot X-ray emitting Intra-group medium (IGrM) (e.g. O’Sullivan et al. 2017). The shallow potential wells of galaxy groups bring galaxies into close proximity, fostering interactions like NGC 1550, NGC 5903 (e.g., Kolokythas et al. 2020; O’Sullivan et al. 2018) or mergers between galaxies (e.g., Pearson et al. 2024). The group scaling relations are known to deviate from self-similarity, suggesting a strong impact of non-gravitational processes such as Active Galactic Nuclei (AGN) feedback in their evolution (e.g. Ponman et al. 1999; Finoguenov et al. 2003; Lovisari et al. 2021).

Galaxy groups provide an important environment where feedback may exert the most significant influence on galaxy formation and evolution (see e.g., Eckert et al. 2021, 2024, for reviews). X-ray bright groups are a key environment for the study of AGN feedback, having almost universally short central cooling times and low entropies (O’Sullivan et al. 2017, 2024). It is known that AGN feedback operates differently in groups (Giodini et al. 2009; Sun 2012), in some cases as a near-continuous ‘bubbling’ mode with moderate thermal regulation (Birzan et al. 2012; Panagoulia et al. 2013; Brienza et al. 2021), in other cases manifesting instead as powerful AGN outbursts (such as the ones sometimes observed in massive clusters), where the group environment is disrupted as in NGC 4261, NGC 193 (e.g., O’Sullivan et al. 2011; Kolokythas et al. 2015, 2018) or gas is stripped (Morganti et al. 2013), at least in the central region due to their shallow gravitational potential. Hence, the group environment represents an excellent opportunity to study a rich array of processes that include galaxy interactions, triggering and quenching of star formation, and the feeding and feedback of the AGN (e.g., Kolokythas et al. 2022; Jennings et al. 2025).

Brightest Group Galaxies (BGGs) serve as excellent laboratories for studying the evolution of galaxy groups and massive galaxies (e.g., Gozaliasl 2016; Gozaliasl et al. 2018). These galaxies are typically highly luminous, old ellipticals located near the centers of the IGrM halo (e.g., Von Der Linden et al. 2007; Stott et al. 2010). Their stellar kinematics span a wide range, from field elliptical-like properties to those resembling BCGs (Loubser et al. 2018; Gozaliasl et al. 2024), and their nuclei host supermassive black holes (e.g., Rafferty et al. 2006). Many BGGs exhibit AGN activity, with some launching powerful radio jets that inject energy back into the IGrM over distances of hundreds of kiloparsecs (e.g., McNamara & Nulsen 2007; Hardcastle & Croston 2020). The fraction of massive galaxies hosting detectable radio emission has increased with survey depth. The LoTSS survey at 150 MHz shows that galaxies with mass  $> 10^{11} M_{\odot}$ , essentially 100% display radio AGN activity above a luminosity threshold of  $L_{150\text{MHz}} \geq 10^{21} \text{ W Hz}^{-1}$  (Sabater et al. 2019), superseding the much smaller sample by Dunn et al. (2010). Earlier, shallower surveys (e.g., Best et al. 2005; Shabala et al. 2008) reported much lower detection fractions ( $\sim 30\%$ ), consistent with their higher flux limits and dif-

ferent sample selections. The Complete Local-Volume Groups Sample (CLoGS) study found a radio detection rates of 92% for the high-richness X-ray bright groups and 87% for the X-ray faint systems (O’Sullivan et al. 2017; Kolokythas et al. 2018, 2019), further highlighting the strong link between radio AGN activity and group environment. In addition to AGN fueling through cooling flows from the IGrM, the link between radio AGN activity and dense galaxy environments (e.g., Lilly et al. 2009; Bardelli et al. 2010; Malavasi et al. 2015) may be influenced by large-scale mergers (e.g., group infall into clusters) or galaxy-galaxy interactions within groups (e.g., Miles et al. 2004; Taylor & Babul 2005). These interactions and mergers can funnel the gas toward the central AGN, triggering radio emission and launching large-scale jets, but are less studied so far due to the dearth of deep enough X-ray observations.

The *XMM-Newton* Group AGN Project (X-GAP<sup>1</sup>, Eckert et al. 2024) seeks to quantify the effects of AGN feedback in a complete sample of 49 galaxy groups, with estimated masses ranging from  $10^{13} \lesssim M_{200} \lesssim 10^{14} M_{\odot}$ , having a narrow redshift range of  $0.025 < z < 0.06$ . These groups have been observed with *XMM-Newton* for a total exposure<sup>2</sup> of approximately 852 ks. They were selected from the ROSAT All-Sky Survey (RASS), and cross-matched with spectroscopic Friends-of-Friends groups from SDSS (Tempel et al. 2017; Damsted et al. 2024). The selection criteria and detailed methodologies are described in Eckert et al. (2024). The X-GAP sample has been observed by LOw Frequency ARray (LOFAR) at 144 MHz (LoTSS; Shimwell et al. 2022). In data release 2 (DR2) and the ongoing analysis for DR3 of LoTSS, images are available for most of the X-GAP groups, providing radio information on both extended and compact emission associated with the BGG (Brienza et al., in prep.).

This paper presents the radio properties of the BGGs of three galaxy groups (Table 1), using new data from the upgraded Giant Metrewave Radio Telescope (uGMRT) observations at 400 MHz, and images from LOFAR 144 MHz observations. We present the properties of the central radio sources, examine their environment, and provide a qualitative comparison between the radio data and X-ray data for each group. The paper is organised as follows: In Section 2, we describe the uGMRT and X-ray observations and the approach followed for the data reduction. In Section 3, we present the radio images and the spectral characteristics of the individual sources, and in Section 4, their X-ray properties (2D thermodynamic maps). Section 5 contains a discussion of our results, focusing on the environmental properties of the radio sources and the spectral index behaviour in those extreme systems. The summary and conclusions are given in Section 6. Throughout the paper, we adopt the  $\Lambda$ CDM cosmology with  $H_0 = 70 \text{ km s}^{-1} \text{ Mpc}^{-1}$ ,  $\Omega_m = 0.27$ , and  $\Omega_{\Lambda} = 0.73$ . All the radio images are corrected for the primary beam attenuation.

## 2. Observations and Data analysis

Three groups were observed with the upgraded GMRT (observation code: 43\_072) (see Table 2). Real-time radio frequency interference (RFI) online filtering, developed to mitigate broadband RFI (Buch et al. 2022, 2023), was applied during the uGMRT observations. The LOFAR observation details are also provided in Table 2.

<sup>1</sup> <https://www.astro.unige.ch/xgap/blog/people>

<sup>2</sup> Exposure time varies per system.

**Table 1.** The list of galaxy groups.

Group	BGG name	RA (deg)	DEC (deg)	Redshift	Velocity dispersion (km s <sup>-1</sup> )	M <sub>200</sub> (10 <sup>13</sup> M <sub>⊙</sub> )	X-ray Luminosity (10 <sup>42</sup> erg s <sup>-1</sup> )	Scale (kpc/arcsec <sup>2</sup> )
SDSSTG8102	MCG+07-33-011	238.76	41.58	0.033	492	15.7 ± 1.4	4.5 ± 1.6	0.662
SDSSTG16393	MCG+09-17-036	152.71	54.21	0.047	295	4.8 ± 0.7	19.6 ± 3.1	0.928
SDSSTG28674	MCG+06-30-029	203.24	32.61	0.037	282	11.9 ± 1.2	4.2 ± 0.9	0.739

**Table 2.** Details of the radio observations and image properties.

Source	Frequency (MHz)	bandwidth (MHz)	Integration time (Hr.)	Beam (arcsec <sup>2</sup> )	Rms noise (μJy beam <sup>-1</sup> )	Source size (kpc × kpc)
SDSSTG8102	144	48	8	8.5 × 8.5	110.0	93.7 × 51.9
	400	200	5	8.5 × 8.5	30.5	72.4 × 51.9
SDSSTG16393	144	48	8	8.0 × 8.0	92.0	119.2 × 82.8
	400	200	5	8.0 × 8.0	32.0	151.0 × 96.1
SDSSTG28674	144	48	8	7.0 × 7.0	85.1	81.5 × 38.6
	400	200	5	7.0 × 7.0	28.7	55.9 × 32.9

## 2.1. LOFAR

The X-GAP targets were observed using LOFAR as part of the LOFAR Two-metre Sky Survey (LoTSS DR2; Shimwell et al. 2017, 2019, 2022). The observations were conducted in High Band Antenna (HBA) dual inner mode, with each target being observed in the field for an 8-hour single pointing. Data reduction and calibration were performed using the standard LoTSS DR2 pipeline (Tasse et al. 2021), which incorporates both the Pre-Factor pipeline (van Weeren et al. 2016; Williams et al. 2016) and the DDF pipeline (Shimwell et al. 2019; Tasse et al. 2021). The Pre-Factor pipeline corrects for direction-independent effects, such as ionospheric Faraday rotation, phase offsets between XX and YY, and clock discrepancies. The DDF pipeline performs direction-dependent calibration to address ionospheric distortions at low frequencies. For improved calibration and re-imaging, the data were processed using the extraction+self-calibration method (van Weeren et al. 2021), in which all sources outside a square region centered on the target were removed from the visibilities, followed by multiple self-calibration loops. The final imaging is done using the WSClean (Offringa et al. 2014).

## 2.2. uGMRT

We processed the uGMRT observations of the three groups using the CAPTURE<sup>3</sup> pipeline (Kale & Ishwara-Chandra 2021), a CASA-based continuum pipeline, specifically developed for the reduction of the GMRT continuum data. After this initial flagging, the flux density of the primary calibrator was set according to the flux scale of Perley & Butler (2017). After following the standard calibration routines and flagging using the automated flagger (tfcrop and rflag), the calibration solutions were applied to the target field, and calibrated target source data were split and further flagged. Special care was taken to remove the narrow-band RFI using the aoflagger (Offringa et al. 2013), and some manual flagging has also been done at the small baselines. To reduce the volume of the data but still prevent bandwidth smearing, the data were averaged to ∼1 MHz frequency resolution. The target visibilities were imaged using the CASA task tclean with wide-field and wide-band imaging algorithms, with nterms=2, and robust = 0. We carried out 5 rounds of

phase only and 3 rounds of phase and amplitude calibration to obtain a good gain solution for the target. For further details on the data analysis procedures for uGMRT, please follow Kale & Ishwara-Chandra (2021); Kale et al. (2022).

## 2.3. Comparison of the flux density scale

The overall flux scale for all observations was verified by comparing the spectra of compact sources within the field of view with those available in the NVSS and TGSS catalogues. The LOFAR 144 MHz data points were already multiplied by a correction factor, mentioned in Shimwell et al. (2022), to match the flux density scale of Scaife & Heald (2012). The uncertainty in the flux density measurements ( $\Delta S$ ) was estimated as

$$\Delta S = \sqrt{(f \cdot S)^2 + N_{\text{beam}} \cdot (\sigma_{\text{rms}})^2}, \quad (1)$$

where  $S$  is the flux density,  $f$  is the absolute flux density calibration error,  $N_{\text{beam}}$  is the number of beams, and  $\sigma_{\text{rms}}$  is the rms noise. We assumed absolute flux density uncertainties of 10% for LOFAR HBA data (Shimwell et al. 2022) and uGMRT (Chandra & Kanekar 2017). The images are corrected for the primary beam using the task `ugmrtpb`<sup>4</sup> for the GMRT.

## 2.4. XMM-Newton

The XMM-Newton observations of these groups were processed using the XMM-SAS software package, version 21, and the X-COP data analysis pipeline (Ghirardini et al. 2019). After applying standard event screening procedures, we extracted light curves from the field of view and the unexposed corners of the three detectors of the European Photon Imaging Camera (EPIC) to remove time periods affected by flaring background. The total good observing time for each group, after filtering out the flaring periods (energy range of 10 – 12 keV, count rate threshold of 0.4 cts/s) is provided in Table 3. For the two MOS detectors, we excluded chips operating in anomalous mode (CCD # 4 for MOS1 and CCD # 5 for MOS2). From the clean event lists, we extracted images from all three cameras in the [0.7–1.2] keV band, which optimises the signal-to-background ratio (Ettori et al. 2012). Effective exposure maps for the three detectors,

<sup>3</sup> <https://github.com/ruta-k/CAPTURE-CASA6>

<sup>4</sup> <https://github.com/ruta-k/uGMRTprimarybeam-CASA6>

**Table 3.** Effective exposure time of each *XMM-Newton* EPIC observation.

Objects	EMOS1 (ks)	EMOS2 (ks)	EPN (ks)
SDSSTG8102	13.8	15.5	8.8
SDSSTG16393	13.5	13.5	13.9
SDSSTG28674	10.9	14.7	18.7

including the telescope's vignetting, were generated using the task `eemap`. The contribution from residual soft protons was estimated using an empirical relation between the difference in high-energy count rates inside and outside the field of view and the soft proton component's normalisation (Salvetti et al. 2017). Finally, we combined the EPIC maps by summing the individual maps from the three detectors, the exposure maps, and the non X-ray background maps. Detailed data analysis procedures of the X-GAP groups have been discussed in Eckert et al. (2025).

### 3. Results: Radio observations

#### 3.1. Continuum Images

Our new multi-frequency images provide a comprehensive view of the radio emission from the central regions of these groups. We have achieved an rms noise of 28 - 32  $\mu\text{Jy beam}^{-1}$  at 400 MHz with uGMRT, and 85 - 110  $\mu\text{Jy beam}^{-1}$  at 144 MHz with LOFAR; LOFAR becomes more sensitive than uGMRT for sources with spectral indices steeper than  $\alpha \leq -1.2$ . We present the uGMRT observations of these groups for the first time. Here, we will discuss the most prominent structures in the various regions of those individual groups.

##### 3.1.1. SDSSTG8102

SDSSTG8102 is the most massive among the three groups in our study (redshift  $z = 0.033$ ), with a mass of  $1.5 \times 10^{14} \text{M}_\odot$ , consistent with a low-mass cluster, and a lower X-ray luminosity, compared to the others (Table 1). The BGG and most of the group members identified from SDSS are early-type galaxies in this group. This group consists of 26 member galaxies with a velocity dispersion of  $\sim 500 \text{ km s}^{-1}$ . We do not see any sign of tidal interactions between the BGG and its nearby companion galaxies.

The uGMRT 400 MHz and LOFAR 144 MHz images (Figure 1, left panel) reveal central radio emission extending several tens of kpc from the group center. At 144 MHz, the morphology suggests two lobe-like features extending northwest and southeast. Higher-resolution and high-frequency data from FIRST (5'') at 1400 MHz (Becker et al. 1994) and VLASS (2.1'') at 3000 MHz (Lacy et al. 2020) show only a patch of diffuse emission, with no identifiable jet or core (green contour from VLASS 2'' resolution in Figure 2). The peak of the radio emission from uGMRT and LOFAR coincides with the BGG of the group. The total emission spans a projected length of  $\sim 93$  kpc at 144 MHz and  $\sim 72$  kpc at 400 MHz, with a projected width of  $\sim 52$  kpc at both frequencies, indicating that uGMRT and LOFAR recover similar spatial scales (using  $3\sigma$  contours as a reference). The emission is predominantly extended, with no compact radio sources embedded within it (Figure 2). Notably, the northern extension bends westward over  $\sim 56$  kpc ( $\sim 85''$ ), suggesting either intrinsic motion of the BGG at the central part of this group toward the east, 'leaving behind' radio emission or an external

factor that has influenced the radio-emitting plasma. While no filamentary substructures are detected at any frequency, the inner region shows a double-peaked brightness structure separated by  $\sim 23$  kpc. The southern peak lies slightly closer to the BGG, which overall appears roughly centered between the two bright spots; the southern feature is more extended, suggesting a projection effect (with the jet axis inclined either in SE–NW direction or toward us). Assuming the jet is oriented in the plane of the sky, the differences between the two peaks would point to varying plasma conditions, likely influenced by the environment. Beyond this double inner structure, the emission gradually fades, except for a sharp drop in surface brightness (by a factor of 5–6) across a  $\sim 10$  kpc ( $\sim 15''$ ) boundary in the southwest. Furthermore, in the uGMRT image, we observe radio emission extending to the northeast, close to source A, up to  $50''$  (33 kpc), with a surface brightness approximately three times fainter than (at  $3\sigma$ ) that of the central radio emission. The source A, adjacent to the extended emission, shows a double structure in the LOFAR and uGMRT images, and has no optical counterpart in the SDSS image; therefore, it is a background radio source.

##### 3.1.2. SDSSTG16393

SDSSTG16393 has the lowest mass among the three,  $4.8 \times 10^{13} \text{M}_\odot$ , and the highest X-ray luminosity (Table 1). This group consists of 46 members and is dominated by early-type galaxies, with relatively high velocity dispersion of approximately  $295 \text{ km s}^{-1}$ . MCG+09-17-036, the (giant elliptical) BGG, is located at  $z=0.047$ , consistent with the group's redshift (Figure 2). UGC 5479, a spiral galaxy at a similar redshift, lies  $\sim 54$  kpc west of the BGG in projection, and while no clear signs of interaction are observed, its proximity may suggest some environmental influence affecting the BGG. Two additional group members, located close to the north and south of the BGG, however, the evidence of interactions is limited with the current data.

The uGMRT 400 MHz and LOFAR 144 MHz images (middle panel, Figure 1) reveal an extended radio source centred on the galaxy group. The morphology includes a bright central region, marginally extended towards the east ( $\sim 20$  kpc), surrounded by more diffuse emission. However, a distinct core–jet–lobe structure is not observed. High-resolution data from VLASS confirm a compact, unresolved core at the BGG position (green contour Figure 2), but no jet-like features or extended lobes are detected at these resolutions and sensitivities. Aside from the core, no additional compact sources are embedded within the diffuse lobe-like region. The surface brightness distribution is smooth, with no identifiable filamentary substructures. It peaks at the centre, coincident with the BGG (Figure 2), and declines gradually toward the outskirts. The uGMRT image shows broadly round morphology with mild elongation along the northeast–southwest axis, whereas the LOFAR image appears more asymmetric, with emission primarily extending north and southwest. The diffuse emission extends up to  $\sim 100$  kpc southwestward in both images, while along the northeast direction, uGMRT recovers slightly more emission ( $\sim 92$  kpc) than LOFAR ( $\sim 82$  kpc).

##### 3.1.3. SDSSTG28674

SDSSTG28674 has a mass of  $1.2 \times 10^{14} \text{M}_\odot$ , and lowest X-ray luminosity among the three groups (Table 1). It is a system that appears to be dominated by several bright galaxies along with one giant elliptical, the BGG, at the center. This group comprises

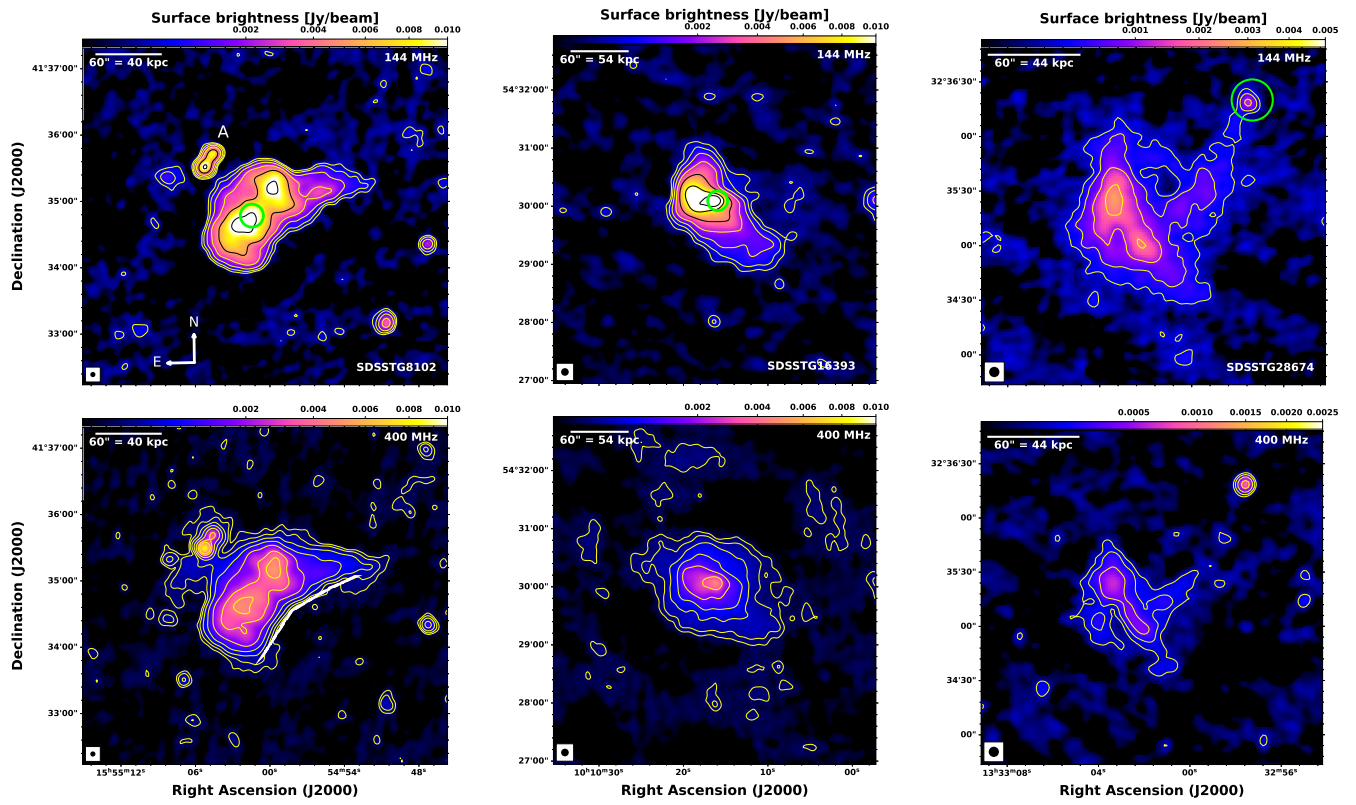


**Fig. 1.** *Left panel:* The LOFAR (upper) and uGMRT (lower) surface brightness maps of SDSSTG8102 are shown in color, and the contours start with  $3\sigma_{\text{rms}} \times [1, 2, 4, \dots]$ , with  $\sigma_{\text{rms}} = 110 \mu\text{Jy beam}^{-1}$  (at 144 MHz), and  $30.5 \mu\text{Jy beam}^{-1}$  (at 400 MHz) respectively. The green circle marks the BGG of the group. The white line in the lower image shows the location of the change in surface brightness. *Middle panel:* The radio surface brightness map for SDSSTG16393 (at 8'' resolution) is shown at both frequencies with a similar contour level as the upper panel, with rms values,  $\sigma_{144\text{MHz}} = 92 \mu\text{Jy beam}^{-1}$  (upper),  $\sigma_{400\text{MHz}} = 32 \mu\text{Jy beam}^{-1}$  (lower). *Right panel:* The same is shown for SDSSTG28674 (at 7'' resolution), with similar contour levels as the left panel with  $\sigma_{144\text{MHz}} = 85.1 \mu\text{Jy beam}^{-1}$  (upper),  $\sigma_{400\text{MHz}} = 28.7 \mu\text{Jy beam}^{-1}$  (lower).

20 galaxy members with a velocity dispersion of  $\sim 300 \text{ km s}^{-1}$ . MCG+06-30-029 is the BGG (lower right panel, Figure 2) situated at a redshift ( $z = 0.0371$ ) similar to that of the galaxy group. We do not see any signs of tidal interaction between the BGG and its nearby companion galaxies.

The uGMRT full-resolution image at 400 MHz and the LOFAR 144 MHz image (lower panel, Figure 1) reveal a compact source associated with the BGG and an extended low-surface-brightness source to the southeast of the BGG. No compact discrete sources are embedded within the diffuse emission, and the radio emission from the BGG is undetected in the VLASS image (green contour Figure 2). In the innermost region of the extended emission, two brightness peaks are observed, separated by  $\sim 20$  kpc and embedded within a broader, mushroom-shaped distribution. The radio emission is elongated along the northeast–southwest axis, with projected sizes of  $\sim 81$  and  $56$  kpc in length, and  $\sim 39$  and  $33$  kpc in width, at 144 and 400 MHz, respectively. At 144 MHz, a faint trail of emission is detected connecting the diffuse structure to the BGG, extending  $\sim 55$  kpc along the northwest–southeast direction. The BGG also shows compact radio emission detected at a significant level ( $\sim 6\sigma$ ), with the peak of optical and radio emissions well coinciding.

### 3.2. Integrated spectrum

We combined our new uGMRT and LOFAR observations with other archival data to investigate the integrated spectral profile of the central diffuse sources. All radio images (LOFAR, uGMRT,

and RACS-Low) were corrected to a common flux density scale using Perley & Butler (2017). The largest angular scale of the diffuse radio emission among the three groups is  $2.79'$ , which is well below the maximum recoverable scales of our data (LOFAR HBA:  $70'$ , uGMRT Band3:  $20' - 30'$ ). As diffuse radio emission in all three groups, apart from the core, is free of compact sources, we estimate the flux density for each group by convolving the radio images to the lowest available resolution across all frequencies, selecting a common area (following a  $3\sigma$  contour) for their flux density measurement. The integrated flux density values are provided in Table 4. The integrated spectra of the radio emission for each group are shown in Figure 3.

SDSSTG8102 displays no evidence of curvature or a spectral break. Given that only three flux density measurements are available (LOFAR, uGMRT, and RACS-low), we do not attempt spectral modelling, since the lack of higher-frequency points prevents meaningful constraints on radiative ageing models. Instead, we estimate the integrated spectral index to be  $-0.96 \pm 0.11$  using these three frequencies. Examining the northwest and southeast components separately, we find similar values:  $-0.92 \pm 0.13$  (northwest) and  $-0.82 \pm 0.11$  (southeast). The radio power of the BGG at 400 MHz is  $4.6 \times 10^{24} \text{ W Hz}^{-1}$ .

The integrated spectral index for SDSSTG16393, between 144 and 400 MHz, is estimated to be  $-1.35 \pm 0.09$ , based on a well-fitted single power law (Figure 3). Although the 3.0 GHz VLA observations (Figure 2) indicate some emission, the VLASS observations are insensitive to angular scales larger than  $\sim 30''$ , and a substantial portion of the extended emission is resolved out. Consequently, the flux density at this frequency is un-

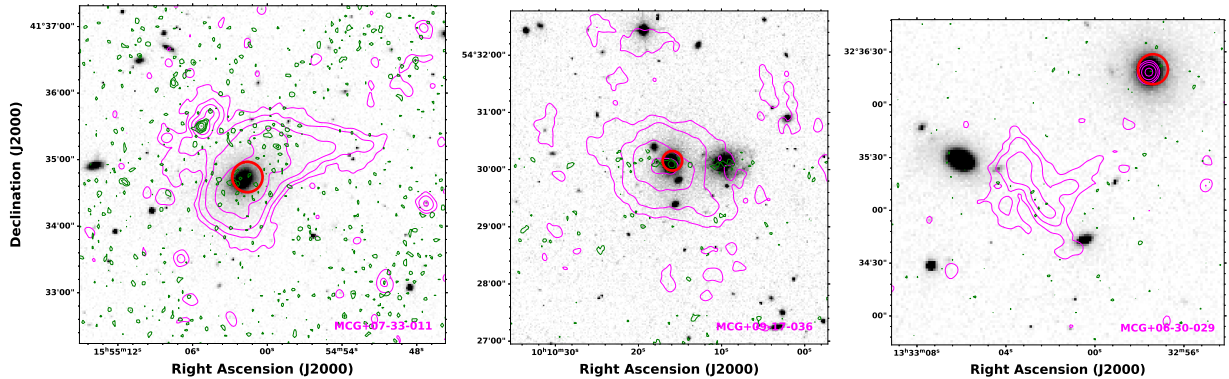


**Fig. 2.** *Left:* The SDSS i-band image of the SDSSTG8102 is shown in colour (grey), and the overlaid magenta contours are from uGMRT 400 MHz, starting with  $3\sigma_{\text{rms}} \times [1,2,4,\dots]$ , where  $\sigma_{\text{rms}} = 30.5\mu\text{Jy beam}^{-1}$ . The green contours are from the VLASS 3.0 GHz image at 2'' resolution, where the contour levels are  $3\sigma_{\text{rms}} \times [1,2,4]$ , with  $\sigma_{\text{rms}} = 108\mu\text{Jy beam}^{-1}$ . The red circle indicates the BGG of the group. *Middle:* The same is shown for the SDSSTG16393, with the same contour level from uGMRT with an rms of  $32\mu\text{Jy beam}^{-1}$ . The green contours are from the VLASS 3.0 GHz map. *Right:* The same is shown for the SDSSTG28674, with the same contour level as the upper panels, with an rms of  $28.7\mu\text{Jy beam}^{-1}$ . The green contours are from the VLASS map, at a similar significance.

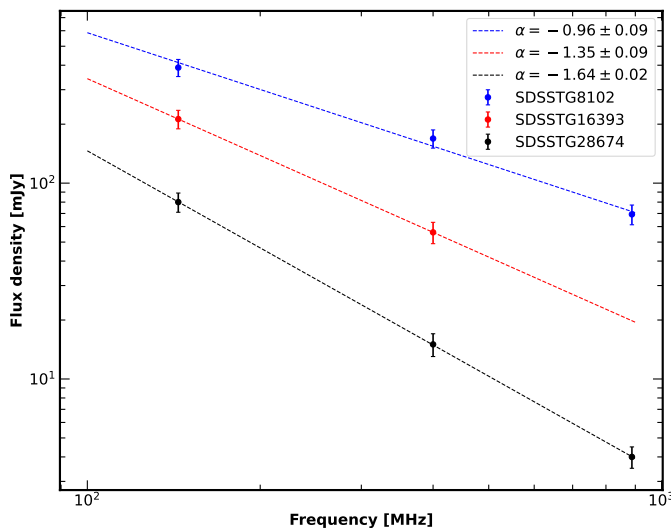


**Fig. 3.** Integrated spectrum of the central radio emission for each of the groups (at different colours) is shown between 144 MHz and 887 MHz. The dashed lines represent the fitted single power law. We have estimated the average flux density from a common region at each frequency for individual groups.

derestimated, and no information about possible high-frequency spectral behaviour can be obtained. The radio power of the BGG at 400 MHz is  $5.1 \times 10^{23} \text{ W Hz}^{-1}$ .

The radio emission (compact radio source associated with the BGG and the extended source) for SDSSTG28674 is well-fitted with a single power law with an integrated spectral index of  $-1.64 \pm 0.02$ , between 144 and 887.5 MHz. The spectral index of the compact source at the BGG between 144 and 400 MHz is  $-0.62 \pm 0.06$ . The radio power at 400 MHz of the BGG is  $7.5 \times 10^{26} \text{ W Hz}^{-1}$ .

### 3.3. Resolved spectral index map

Spatially resolved spectral indices provide valuable insights into the particle acceleration mechanisms behind group-scale extended radio AGN (e.g., [Kolokythas et al. 2020](#); [Rajpurohit et al. 2024](#); [Pasini et al. 2025](#); [Riseley et al. 2025](#)). Using the 400- and 144-MHz images, we produced a resolved spectral index

**Table 4.** Flux density estimates for radio sources of each group.

Source	Freq.	Flux density (mJy)	Ref.
SDSSTG8102	144	$389.07 \pm 39.00$	This work
	400	$184.94 \pm 18.00$	This work
	887.5	$64.29 \pm 8.00$	RACS-low
SDSSTG16393	144	$212.33 \pm 23.00$	This work
	400	$62.07 \pm 7.00$	This work
	887.5	$15.02 \pm 2.00$	This work
SDSSTG28674	144	$80.03 \pm 9.00$	This work
	400	$15.02 \pm 2.00$	This work
	887.5	$4.00 \pm 0.50$	RACS-low

**Notes.** References for the RACS-low is [McConnell et al. \(2020\)](#); [Hale et al. \(2021\)](#).

map for the extended emissions in each group. These spectral index maps were generated by convolving each image to a common resolution, which enhances the signal-to-noise ratio (S/N) of the extended emission and preserves any small-scale features that would otherwise average out. The procedure for creating the spectral index maps follows the method described in [de Gasperin et al. \(2017\)](#), where the spectral index values were estimated as the logarithmic ratio of the two images, and to estimate the uncertainties, the flux density values of each pixel are obtained 1000 times from a Gaussian distribution that has the same mean as the estimated flux density value and the same standard deviation as the background rms of the images. The individual properties and a detailed discussion of the spectral index maps are presented below for individual groups:

**SDSSTG8102:** The spectral index map appears to be relatively uniform throughout the extent of the emission (Left panel Figure 4). In the central region, the average spectral index ranges from  $\sim -0.7$  to  $-0.9$ . This general spectral index distribution aligns with the integrated spectral index measurement for total diffuse emission (Section 3.2). Different spectral indices are observed for the inner bimodal surface brightness distribution, with the southern part showing an average spectral index of  $\sim -0.94 \pm 0.09$  and the northern part showing  $\sim -0.75 \pm 0.11$ . The flatter spectral indices suggest that these regions are predominantly filled with younger radio plasma. At the BGG location, the spectral index is mainly uniform with  $\sim -0.7$ . The northwest extension also exhibits a uniform spectral index of  $\sim -0.75$ . The spectral index error ranges from  $\sim 0.01$  near the core to  $\sim 0.1$  in

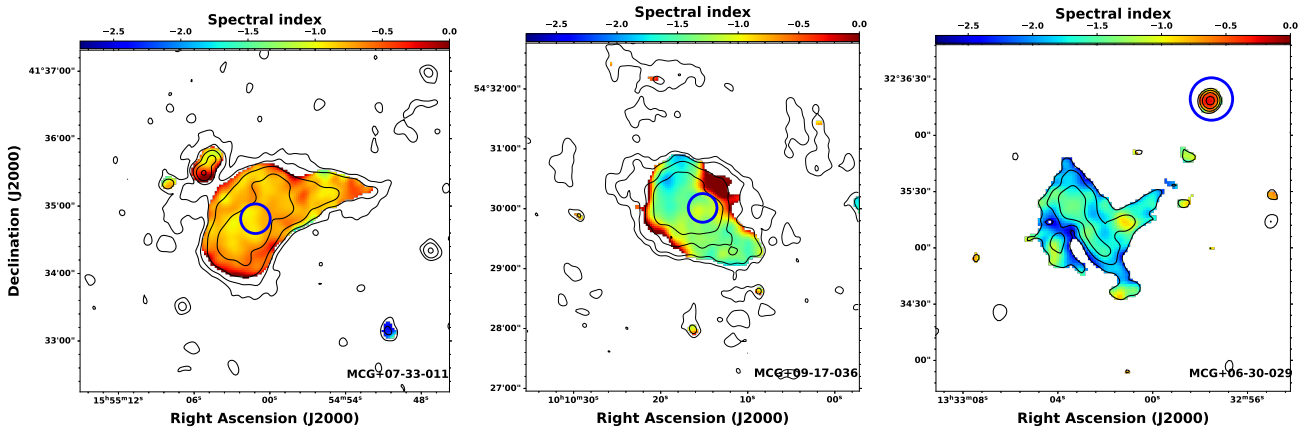


**Fig. 4.** *Left:* The spectral index map between 144 and 400 MHz is shown for SDSSTG8102. The overlaid black contours are from uGMRT 400 MHz, starting with  $3\sigma_{\text{rms}} \times [1, 2, 4, \dots]$ , where  $\sigma_{\text{rms}} = 30.5 \mu\text{Jy beam}^{-1}$ , and the blue circle indicates the BGG of the group. *middle:* The spectral index map is shown for SDSSTG16393. The contour level is similar to the upper panel, and the  $\sigma_{\text{rms}} = 32 \mu\text{Jy beam}^{-1}$ . *Right:* The same is shown for SDSSTG28674, having similar contour levels, with an  $\sigma_{\text{rms}} = 28.7 \mu\text{Jy beam}^{-1}$ .

the outer regions (shown in Figure A.1, see Appendix A for the spectral index error maps).

**SDSSTG16393:** The spectral index map for the extended emission does not show any clear trends or small-scale features (middle panel, Figure 4). However, the overall spectral index distribution is steep (below  $-1.0$ ) over the extent of the emission from the southwest to the northeast. In the core region, surrounding the BGG, the average spectral index is  $\sim -1.0$ , while in other parts of the extended emission, the spectral index steepens to  $\sim -1.6$ . We observe a steepening of the spectral index moving from the central region to outwards. Such a steep spectrum suggests that these regions may contain considerably older radio plasma, possibly originating from some remnant radio lobes. The error in the spectral index ranges from  $\sim 0.01$  near the core to  $\sim 0.2$  in the outer regions. However, the errors in the southwest part are higher compared to northern part.

**SDSSTG28674:** The spectral index distribution shows spatial variations (right panel, Figure 4). In particular, the spectral index steepens toward the eastern part of the emission, while remaining relatively uniform ( $\sim -1.5$ ) along the northeast–southwest axis. A notably steeper region, with a spectral index of  $\sim -1.9$ , is observed surrounding the main streak. The BGG itself exhibits a flatter spectral index, averaging greater than  $-0.5$ , contrasting with the diffuse emission, which generally has a steeper index of  $\sim -1.6$ , consistent with the integrated spectral index (Section 3.2). Additionally, a patch with a spectral index of  $\sim -1.0$  is located at the junction of the ‘L’-shaped structure, although no associated galaxy or point source is found at that position. Overall, the spectral index errors range from  $\sim 0.05$  in the brighter central regions to  $\sim 0.25$  in the outskirts.

## 4. Results: X-ray observations

This section presents the X-ray surface brightness maps from the *XMM-Newton* for the three galaxy groups. Their individual properties, along with the detailed description of the thermal emission, are discussed as follows:

### 4.1. Surface brightness map

**SDSSTG8102:** The *XMM-Newton* observation of this galaxy group reveals a disturbed morphology of the diffuse emission from the IGrM (left panel, Figure 5). The extended emission is

elongated along the east–west direction, with a projected size of approximately 300 kpc, and the overall shape of the emission is asymmetric. The brightest X-ray emission is closely aligned with the position of the BGG. However, another bright compact source is located about 40 kpc away from the BGG in the northeast direction, and the inner surface brightness distribution shows slight elongation in that direction, suggesting some interaction between the two. An extended feature is visible on the eastern side (white arrows); however, the resolution of the current *XMM-Newton* image limits the ability to analyse for any potential surface brightness edge. The peak of the radio emission is coincident with the X-ray peak, and the radio emission at both frequencies is confined to the group core. Morphologically, the central X-ray emission is elongated eastward, while the radio emission is oriented in the northwest direction.

**SDSSTG16393:** X-ray observations of this group reveals disturbed IGrM emission (Figure 5, middle). The diffuse morphology, elongated northward ( $\sim 250$  kpc), forms a broad triangular shape with the brightest peak centred on the BGG. A second bright group galaxy,  $\sim 150$  kpc west of the BGG, may indicate a group-scale interaction or gravitational influence, driving the asymmetry. On the eastern side of the BGG, a sharp surface brightness drop by a factor of 2–3 is observed across  $\sim 18$  kpc (white arrows). Further south, at 398 kpc away from the BGG, a  $\sim 700$  kpc patch of extended diffuse X-ray emission is detected (Appendix B), hosting three bright unresolved sources but no clear link to a concentrated galaxy population. Although some galaxies in this region share the group redshift, the nature of the emission remains uncertain, potentially linked to a separate infalling group.

The radio morphology closely follows the thermal emission, with both 144 and 400 MHz emission largely confined to the core. At 144 MHz, the emission extends northward, similar to the X-ray distribution, but is bounded on the eastern side by a sharp edge where the inner jet structure is deflected along northward; beyond this boundary, no 144 MHz emission is seen. However, at 400 MHz, some emission is detected past this edge.

**SDSSTG28674:** The X-ray emission from this group reveals two peaks and a disturbed IGrM. The diffuse emission is elongated along the northwest–southeast axis, spans  $\sim 350$  kpc in projection, and exhibits an overall elliptical morphology. The IGrM bridges the two galaxy cores and aligns with the inferred merger axis. Of these, the northwest galaxy is the BGG, while

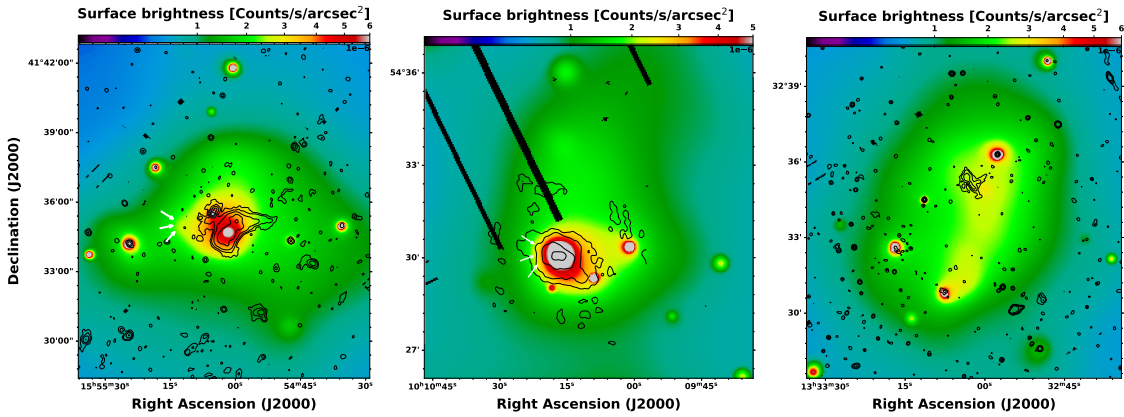


**Fig. 5.** *Left:* Adaptively smoothed 0.7 – 1.2 keV image from the *XMM-Newton* is shown in color for SDSSTG8102, and the overlaid contours are from uGMRT 400 MHz, starting with  $3\sigma_{\text{rms}} \times [1,2,4,\dots]$ , with  $\sigma_{\text{rms}} = 30.5\mu\text{Jy beam}^{-1}$ . *Middle:* The same is shown for the SDSSTG16393 at 0.7 – 1.2 keV range, with similar contour spacings, starting with an rms of  $32\mu\text{Jy beam}^{-1}$ . The black strips are the chip gaps for the *XMM-Newton* CCDs. *Right:* The X-ray map is shown for the SDSSTG28674, with the same contour level as the previous panels, with an rms of  $28.7\mu\text{Jy beam}^{-1}$ .

the southeast galaxy is a spectroscopically confirmed member ( $z \sim 0.0359$ ), supporting the scenario of an internal group merger rather than a projection with a background system. Although multiple galaxies are visible in the SDSS i-band image, most of them are not detected in X-rays.

Compact radio sources are detected coincident with the BGG and the dominant galaxy of the southern core. The extended radio structure is not coincident with any group member, and does not seem to be associated with any definite IGrM structure, although it lies close to the merger axis. The X-ray emission is significantly extended beyond the radio emission, and much of the thermal gas lacks corresponding radio emission.

#### 4.2. 2D thermodynamical maps

We applied the Adaptive Circular Binning (ACB) algorithm to map the 2D distribution of projected IGrM thermodynamical properties. Spectra were fitted with an absorbed APEC model, with hydrogen column density fixed to the Galactic value and abundance to 0.3  $Z_{\odot}$ . Background spectra were taken from source-free CCD regions and supplemented with ROSAT All-Sky Survey data, with a model (local hot bubble, Galactic halo, cosmic X-ray background) jointly fitted to EPIC and RASS spectra. The procedure for producing *XMM-Newton* temperature maps is detailed in Botteon et al. (2024). The properties of the individual groups are discussed below.

**SDSSTG8102:** The 2D temperature and pseudoentropy distributions for this group are shown in Figure 6 (left). The temperature distribution is non-uniform with localised high-temperature patches. The central regions have an average temperature of  $\sim 1.40$  keV, decreasing to  $\sim 1.15$  keV along northward, while toward the east it remains uniform at  $\sim 1.50$  keV. Some central regions show a temperature  $\sim 2$  keV. Temperature errors are  $\sim 8\text{--}12\%$  in the core, rising to  $\sim 17\%$  along eastward. The pseudoentropy map also shows largely uniform distributions, with a minimum of  $35 \text{ keV cm}^2$  at the core (uncertainty  $\sim 10\%$ ). Overall entropy rises to  $\sim 50 \text{ keV cm}^2$  in the northward and  $\sim 60 \text{ keV cm}^2$  in the eastward, with uncertainties of  $\sim 13\%$ .

The radio emission, overlaid on the temperature map, lies in a region of largely uniform temperature, though smoothing from the adaptive binning algorithm may affect fine-scale variations. The radio peak coincides with a low entropy region. The southern part of the source has a slightly higher average temperature

( $\sim 1.53$  keV) than the northern part ( $\sim 1.30$  keV), but the difference is within  $2\sigma$ . Most of the radio emission is co-spatial with regions of entropy  $\sim 35 \text{ keV cm}^2$  along the western side, while the lobes also extend into higher-entropy regions (50–55  $\text{keV cm}^2$ ).

**SDSSTG16393:** The X-ray surface brightness distribution of this group shows elongated emission toward the north, consistent with the thermodynamic maps (Figure 6; middle panel). The temperature distribution is non-uniform, marked by several high-temperature patches. In the central regions, the average temperature is slightly lower ( $\sim 1.15$  keV) than in the surroundings, while toward the north it rises to  $\sim 1.7$  keV. The elongation of the X-ray emission in this direction is accompanied by high-temperature gas. Near a discrete source close to the centre on the southwest side, a patch of hotter gas reaches to  $\sim 2.1$  keV. Temperature uncertainties remain relatively uniform ( $\sim 8\text{--}12\%$ ) near the core, increasing northward up to  $\sim 20\%$ . The pseudoentropy map shows a central minimum of  $25 \text{ keV cm}^2$  (uncertainty  $\sim 9\%$ ), rising along northward to  $\sim 80 \text{ keV cm}^2$  with uncertainties of 10–13%.

When overlaid on the temperature map, the radio emission coincides with a cool patch extending northwest from the BGG, and with hotter emission along the northeast and southwest. However, the core is relatively cool, and the temperature rises to  $\sim 1.25$  keV at  $\sim 60$  kpc, matching the radio extent. The brighter radio emission is co-located with the low-entropy central regions, and along the southwest direction, the temperature increase is accompanied by an entropy rise to  $\sim 50 \text{ keV cm}^2$ .

**SDSSTG28674:** Figure 6 (right) shows the temperature map of this group from *XMM-Newton* multi-band images. The temperature distribution is not azimuthally symmetric: the coolest regions (0.8–1.0 keV) lie near the northwest BGG, while no such low-temperature regions are seen around the southeast galaxy. The average IGrM temperature is  $\sim 1.4$  keV, with patches of slightly lower values ( $\sim 1.1$  keV). Pockets of higher temperature suggest interactions or heating of the gas, consistent with the X-ray surface brightness map (Figure 5). The pseudoentropy map shows the lowest values at the BGG ( $\sim 30 \text{ keV cm}^2$ ), rising to  $\sim 50\text{--}60 \text{ keV cm}^2$  in the surroundings. No clear trend is seen along the merger axis, though some low-temperature regions exhibit higher entropy than their surroundings. Typical uncertainties are 5–10% in the core, increasing beyond 20% at larger radii due to low S/N. The diffuse radio structure coincides with a small cool region, southwest of the BGG.

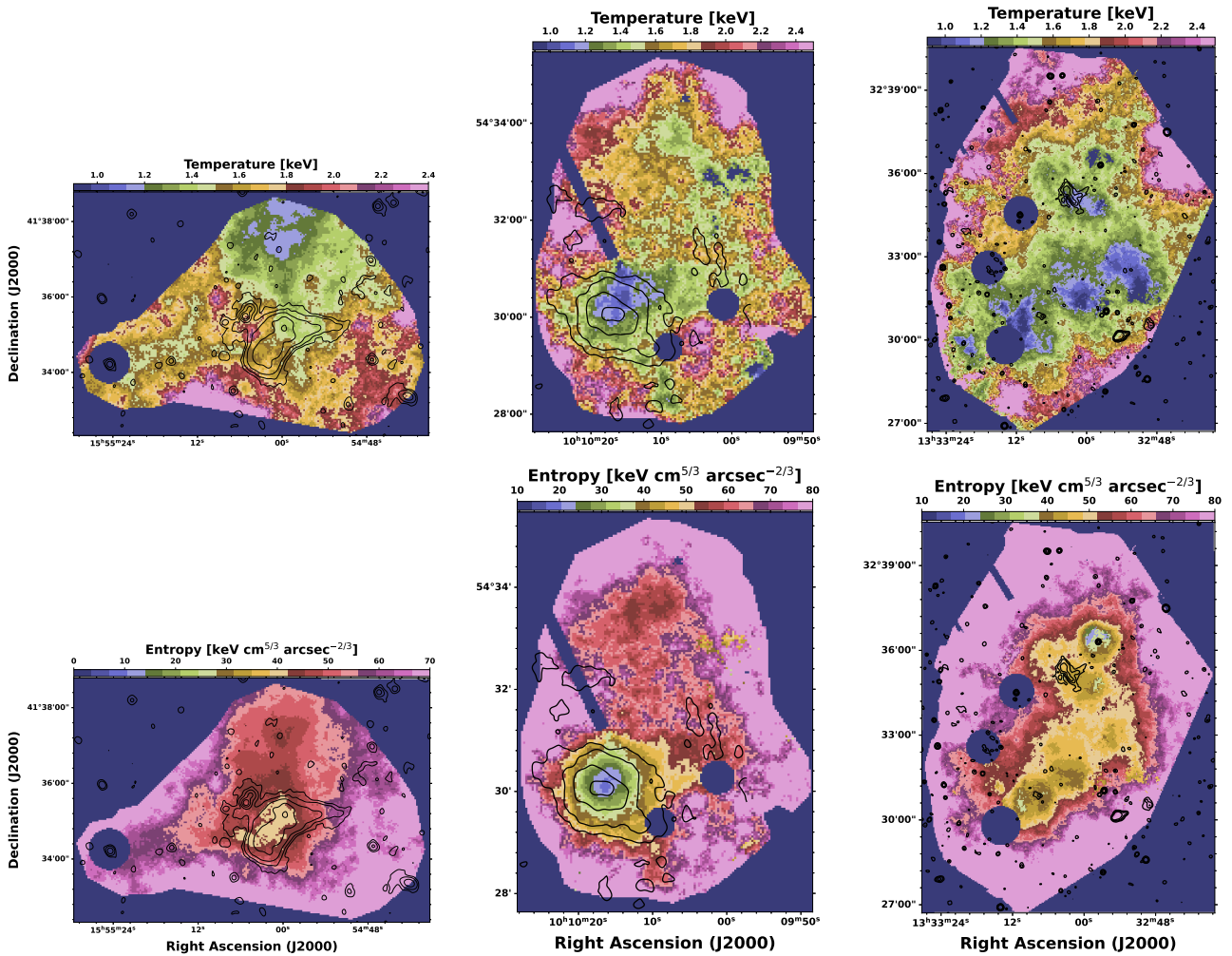


**Fig. 6.** *Left:* The 2D temperature (upper) and corresponding entropy map (below) is shown for SDSSTG8102. The overlaid yellow contours are from uGMRT 400 MHz radio emission, starting with  $3\sigma_{\text{rms}} \times [1, 2, 4, \dots]$ , where  $\sigma_{\text{rms}} = 30\mu\text{Jy beam}^{-1}$ . *Middle:* The temperature and entropy maps are shown for the group SDSSTG16393. The contour level is similar to the upper panel with an rms noise of  $\sigma_{\text{rms}} = 32\mu\text{Jy beam}^{-1}$ . *Right:* The same is shown for SDSSTG28674, having similar for the contour levels, with an  $\sigma_{\text{rms}} = 28.7\mu\text{Jy beam}^{-1}$ .

## 5. Discussion

In this paper, we focus on three galaxy groups from the X-GAP sample, presenting the detailed radio and X-ray analyses of their diffuse emission. The three groups are dynamically disturbed, and the radio emission in and around the BGG shows the signatures of an aged relativistic plasma. These three groups form the first part of our detailed investigation of the entire X-GAP sample. We present an interpretation of the individual systems and discuss their properties in the context of the other well-studied groups and samples.

### 5.1. BGGs in the three groups

**SDSSTG8102:** The BGG hosts radio emission extending to  $\sim 90$  kpc, with clear signs of northwest lobes being displaced westward by the motions of IGrM. Such features are not unusual, but they indicate that the group core is not fully relaxed. The BGG often shows peculiar velocities comparable to, or even slightly exceeding, the group velocity dispersion (e.g., [Gozaliasl et al. 2020](#)). The uGMRT images reveal additional extensions toward the southwest and an overall westward bend of the lobes, both consistent with IGrM flows drawing out the radio plasma.

This interpretation is supported by the *XMM-Newton* images, which show the gas density elongated along the east–west axis. The uGMRT maps, however, reveal that the lobes extend to the northeast, which does not neatly fit this picture. In dynamically active systems, bulk IGrM motions can distort the radio lobes and promote energy redistribution. Simulations ([Bourne et al. 2019](#); [Bourne & Sijacki 2021](#)) show that such motions enhance mixing between jet plasma and the ambient gas, leading to more isotropic and efficient heating, effects that may also be operating here. The emission has a steep spectrum ( $\alpha \sim -0.9$ ), implying the presence of an aged relativistic electron population.

**SDSSTG16393:** The BGG hosts central radio emission beyond 100 kpc. The uGMRT image reveals a nearly symmetrical source with a slight SW–NE extension, while the LOFAR map highlights a distortion on the northern side, suggesting displacement by motions of the IGrM. This interpretation is also supported by the X-ray data, where a drop in surface brightness (white arrow in Figure 5) is observed at the same location, indicating that the gas motions may be affecting the radio plasma. The temperature map reveals hotter regions toward the SW, coinciding with the radio extent and suggesting local IGrM heating by the radio source, similar to what has been reported from numerical simulations by [Bourne & Yang \(2023\)](#). The emission has

a steep spectrum ( $\alpha \sim -1.6$ ), consistent with an aged relativistic electron population, most plausibly the remnant lobes of past AGN activity.

**SDSSTG28674:** The BGG, located at the northern peak among the two X-ray peaks in the group, hosts a compact source linked by a faint bridge to an extended source. One interpretation is that it represents a single lobe connected to the BGG by a fading jet, with the absence of a counter-lobe explained by gas motions from the ongoing merger compressing and re-energising only one side (e.g., [Randriamanakoto et al. 2020](#); [Shulevski et al. 2024](#)). Alternatively, the emission could trace an old pair of lobes deposited in a previous cycle of activity, now connected back to the BGG by a faint trail as the galaxy moved (similar to NGC 5419; [Subrahmanyan et al. 2003](#)). The steep spectral index also raises the possibility of a radio phoenix, where fossil plasma is revived by compression or shocks in the IGrM, similar to the ultra-steep phoenix in Abell 2877 ([Hodgson et al. 2021](#)). Another scenario is that the BGG has drifted away from the centre of a once-symmetric source (e.g., [Shulevski et al. 2024](#)), as observed in offset remnants such as 3C 338 ([Timmerman et al. 2022](#); [Antas et al. 2024](#)). In all cases, the link with the merger axis suggests that the group's dynamical state has strongly influenced the emission, making this an intriguing example of IGrM-driven radio morphology. Further data, especially polarisation, is required to distinguish between a re-energised lobe and a remnant structure.

## 5.2. Comparison with other groups

### 5.2.1. Presence of extended lobes

Extended radio emission is increasingly being observed in galaxy groups, providing important insights into the interaction between AGN outflows and the IGrM (e.g., [Schellenberger et al. 2017](#); [Kolokythas et al. 2020](#); [Rajpurohit et al. 2024](#); [Pasini et al. 2025](#); [Brienza et al. 2025](#)). BGGs are detected in the radio more frequently than the general galaxy population (e.g., [Grossová et al. 2022](#); [Wójtowicz et al. 2023](#)), but comparisons across group samples must be made with caution, as selection criteria differ in redshift, luminosity, and other parameters.

Detecting extended diffuse emission in groups requires high sensitivity and angular resolution, since such features are faint and relatively uncommon ( $\sim 9\%$  or  $5/53$  in the local Universe; [O'Sullivan et al. 2017](#); [Kolokythas et al. 2019](#)). [Kolokythas et al. \(2019\)](#) argues that their presence depends primarily on the X-ray properties of the group core (e.g., cool cores fueling AGN) and the nature of the BGG, with less influence from the stellar population mix. Within the CLoGS sample ([Kolokythas et al. 2018, 2019](#)), diffuse radio sources are found in both spiral-rich and spiral-poor groups, ranging from remnant jets to amorphous lobes. In the three systems studied here, two sources (SDSSTG8102 and SDSSTG16393) show morphological alignments between their extended radio and X-ray emission, and both are elongated along the same axis (Figure 5). No cavities or shocks are seen, possibly due to the sensitivity limits of current X-ray data, but both sources host central diffuse emission coincident with the BGG. High-resolution maps reveal compact cores in SDSSTG16393, but no clear jets. Both broadly resemble a central radio galaxy, with distortions suggestive of IGrM bulk motions. In contrast, SDSSTG28674 hosts a more unusual source, offset from the BGG by  $\sim 63$  kpc and lacking a compact AGN core or symmetric lobes. A faint 144 MHz bridge connects the diffuse emission to the BGG, but the strongly one-sided morphology remains puzzling. Comparisons to systems such as

NGC 677 and NGC 5903 in CLoGS ([Kolokythas et al. 2018](#); [O'Sullivan et al. 2018](#); [Kolokythas et al. 2019](#)) highlight both similarities and differences: the X-GAP sources extend to larger scales (80–120 kpc) and often lack classical jet–lobes morphologies, resembling remnant jet systems like NGC 1407 but showing greater structural diversity. Overall, these results suggest that diffuse central radio sources in groups can arise through multiple pathways: direct AGN outbursts, buoyantly rising lobes, or phoenix-like revivals of fossil plasma. The detection of such extended diffuse structures in both the CLoGS and X-GAP samples suggests that their appearance requires specific environmental conditions. The conditions may depend not only on whether the group is relaxed or merging, but also on the interplay between the AGN activity, IGrM, and the large-scale group dynamics.

### 5.2.2. Spectral index distribution

Spectral index provides a powerful insight into the age and energetics of the radio plasma, as well as the environmental processes that shape its evolution (e.g., [Lisenfeld & Völk 2000](#); [Konar et al. 2006](#); [Jamrozy et al. 2008](#)). While compact AGN cores often display flat spectra due to synchrotron self-absorption and ongoing particle injection, extended lobes and diffuse components generally steepen over time as radiative and adiabatic losses dominate (e.g., [McKean et al. 2016](#)). In dense group environments, surrounding IGrM can confine the plasma and prolong the visibility of steep-spectrum lobes ( $\alpha \sim -1$  to  $-2$ ; [Giacintucci et al. 2011](#)), whereas in lower-density environments the plasma expands more freely, leading to faster fading of relic structures (e.g., [Stewart et al. 2025](#)).

Across the three X-GAP systems, we find a clear diversity in the spectral behaviour, reflecting different stages of AGN life cycles. SDSSTG8102 exhibits a spectral index of approximately  $-0.9$ , which is steep, and some radio remnants have been observed with similar spectra below 1 GHz (e.g., [Brienza et al. 2016, 2017](#)). The BGG in SDSSTG8102 remains a candidate remnant radio galaxy. In contrast, the BGG in SDSSTG16393, the spectrum is much steeper ( $\alpha \lesssim -1.0$ ), characteristic of a strongly aged synchrotron plasma and indicative of fading activity. The BGG in SDSSTG28674 shows a flat spectrum core emission, with an extended lobe having a very steep spectrum ( $-1.74$ ), indicating a restarted system, where an active core coexists with extended, aged emission from a previous activity cycle. The BGG in SDSSTG16393 shows classical ultra-steep-spectrum characteristics consistent with an evolved remnant; the other two represent earlier or more complex remnant phases. For SDSSTG8102, although the low-frequency spectral index (144–400 MHz) is not ultra-steep, it is already relatively steep given the frequency range probed, and the absence of compact features, jets, or a radio core, together with the amorphous morphology, suggests that large-scale jet activity has ceased. This source is therefore consistent with a young remnant, in line with both observational studies and simulations predicting a population of remnants whose spectral break lies at higher frequencies. SDSSTG28674 likely represents a restarted system, where an active core coexists with extended, aged emission from a previous activity cycle. This spread implies the coexistence of different remnant phases of central radio sources in groups, with the spectral properties strongly shaped by duty cycle and the availability of gas to fuel the activity. In CLoGS sample it was found that, while typical integrated spectral indices in X-ray bright groups lie around  $-0.6$  to  $-0.9$ , systems with spectral index of  $\alpha_{235}^{610} = -1.38 \pm 0.07$  and  $\alpha_{235}^{1400} = -1.11 \pm 0.07$  were also found ([Kolokythas et al. 2019](#)). The ultra steep indices ( $\lesssim -1.0$ )

in two of our X-GAP groups (SDSSTG16393, SDSSTG28674) are consistent with this latter class.

Another key trend observed in the CLoGS sample is that large-scale jet ( $\gtrsim 50$  kpc) systems show distinct spectral properties based on their evolutionary stage and interaction with the surrounding medium. Environmental factors, such as jet bending or confinement by IGrM, can also contribute to spectral steepening (Kolokythas et al. 2018, 2019). This supports the idea that a combination of source age, AGN history, and environmental conditions plays a central role in shaping the spectral evolution of radio sources in galaxy groups, as is seen in the three X-GAP groups.

### 5.2.3. X-ray environmental effects

The X-ray environment plays a key role in shaping the morphology and energetics of the group-central radio galaxies (e.g., Shin et al. 2016; Liu et al. 2019). In all three X-GAP systems, the IGrM is bright and extended to  $\sim 300$  kpc, and each hosts a central radio source with emission exceeding 50 kpc in length. These emissions remain confined within the X-ray halos, supporting the idea that dense hot gas both stabilises the radio outflows and provides a reservoir for AGN fueling. Energy transfer from the jets to the IGrM—through shocks, turbulence, or cosmic ray diffusion—may help to offset the radiative cooling and maintain thermal balance (Fabian 2012; Eckert et al. 2021; Hlavacek-Larrondo et al. 2022). This agrees with the CLoGS survey, where jet-mode AGN are almost exclusively found in X-ray bright groups (Kolokythas et al. 2018), while X-ray faint groups usually host only compact or weak radio sources. Such an environmental dependence suggests that a substantial hot gas halo is essential for sustaining large-scale radio-mode AGN activity, most likely via cold chaotic accretion (CCA; Gaspari et al. 2013, 2019), but alternative fueling processes remain possible.

Mergers disturb the IGrM, enhancing the turbulence and mixing, and potentially triggering multiphase gas condensation and SMBH fueling (e.g., Brienza et al. 2022; Shulevski et al. 2017). Although major group–group mergers are rare, typically occurring on  $\sim 5$ –6 Gyr timescales (Rodriguez-Gomez et al. 2015; Pasini et al. 2021; Sharma et al. 2024), their signatures are evident in these X-GAP groups. Each of the three X-GAP groups shows elongated X-ray halos or asymmetric distributions, accompanied by correspondingly distorted radio structures. This morphological coupling suggests that merger-driven gas motions have played a role in shaping both the thermal and non-thermal components. In particular, one system shows radio jets aligned with an elongated X-ray halo, another exhibits asymmetric lobes within a disturbed north–south gas distribution, and a third reveals diffuse, fading emission coincident with a binary group merger. Together, these lead to an evolutionary sequence where mergers initially drive gas inflows that enhance AGN activity, followed by fading radio structures as fueling diminishes. Another physical aspect is that large-scale, bright radio lobes cannot be sustained without confinement by a substantial hot halo. The X-ray emitting IGrM provides the dominant external thermal pressure; if the internal lobe pressure greatly exceeds this value, the lobes will expand supersonically and rapidly fade until equilibrium is reached. Since radio surface brightness traces the line-of-sight non-thermal pressure, while X-ray brightness traces the integrated thermal pressure, richer X-ray environments naturally host brighter and more extended radio lobes, even when the fueling mechanisms are similar.

Compared with CLoGS systems that experienced gas-poor (dry) mergers and lack extended radio emission (e.g.,

Kolokythas et al. 2019), the X-GAP groups stand out as gas-rich, dynamically active environments capable of sustaining large-scale diffuse structures. The differences could be due to different sample selection strategies, as CLoGS targets nearby, optically-selected groups with evolved BGGs, while X-GAP preferentially includes X-ray bright systems, where residual gas reservoirs are still present. Therefore, merger type plays a crucial role in shaping the radio properties of galaxy groups, and some mergers produce diffuse emission, and others do not. This suggests that the presence of large-scale jets depends on the environment, the group’s evolutionary stage, the nature of the merger itself, and the efficiency of the gas accretion on the central SMBH. The three merging X-GAP groups offer a valuable opportunity to refine our understanding of these processes, especially by revealing merging systems with diffuse emission rarely observed.

## 6. Summary

We present the results from the uGMRT 400 MHz observations for the three X-GAP galaxy groups. These sensitive uGMRT observations at 400 MHz enable us to obtain detailed spectral characteristics of the central extended sources by combining them with LOFAR observations at 144 MHz. Our radio results, corroborated with available X-ray observations (*XMM-Newton*), provide profound physical insights into the thermal and non-thermal connections in the IGrM. The overall findings are summarised below:

1. All three groups show large-scale lobes spanning from  $\sim 50$  – 150 kpc at both 400 and 144 MHz. Double-lobed radio emission is associated with the BGG for two groups, except SDSSTG28674, where the BGG hosting a compact radio source is connected with the extended emission with a faint bridge of emission.
2. The radio emission in SDSSTG8102 follows a single power law with an average spectral index of  $\sim -0.9$ , consistent across its northern and southern components, and shows a uniform distribution ( $\sim -0.8$ ) in the spectral index map. SDSSTG16393 has an integrated spectral index of  $\sim -1.2$  (144–400 MHz) and a spatially varying spectral index, with steeper values ( $\sim -1.6$ ) in the outskirts and a slightly flatter index ( $\sim -0.95$ ) in the central region. SDSSTG28674 has the steepest integrated spectrum of  $-1.75$ , indicative of a rapidly fading remnant lobe that is undetected at higher frequencies.
3. The X-ray maps reveal elongated morphologies in all three groups, with SDSSTG28674 showing clear signs of a binary merger. No cavities or discontinuities are detected, likely due to the limited depth of the *XMM-Newton* data. In SDSSTG8102 and SDSSTG16393, the central radio emission aligns well with the X-ray emission and BGG position.
4. We present 2D thermodynamic maps of the groups, highlighting the thermal structure of the IGrM. SDSSTG8102 shows an average central temperature of  $\sim 1.4$  keV, increasing to  $\sim 1.5$  keV toward the west. SDSSTG16393 has a cooler core ( $\sim 0.9$  keV) with a hotter region ( $\sim 1.7$  keV) to the north, where the gas temperature increases up to 60 kpc from the center toward the radio emission. SDSSTG28674 exhibits signatures of merging activity, with the BGG region at 0.7 – 1.0 keV and hotter gas ( $\sim 1.5$  keV) along the merger axis.
5. We discuss similarities of each of these systems with other groups that have been studied earlier regarding their linear extents, spectral index distribution, and X-ray properties.

6. This study showcases the behaviour of radio emission associated with the BGGs in merging galaxy groups. In the future, the study will be extended to the complete sample of 49 groups in X-GAP.

In conclusion, our multi-wavelength study of three merging galaxy groups, using uGMRT, LOFAR, and *XMM-Newton*, reveals significant insights into the interplay between AGN activity and the IGrM. The radio emission observed in these groups appears to be influenced by interactions with the surrounding IGrM. The X-ray and radio emissions show distinct correlations, providing evidence for the complex processes at play in these merging systems. The findings highlight the importance of environmental conditions in shaping the radio properties and evolution of galaxy groups. These results motivate deeper multi-wavelength follow-up of X-GAP groups to confirm the presence of cold gas and test whether wet merger signatures consistently accompany large-scale AGN feedback.

**Acknowledgements.** We thank the anonymous referee for their constructive comments that have improved the clarity of the paper. R.S. and R.K. acknowledge the support of the Department of Atomic Energy, Government of India, under project no. 12-R&D-TFR-5.02-0700. MB acknowledges financial support from Next Generation EU funds within the National Recovery and Resilience Plan (PNRR), Mission 4 – Education and Research, Component 2 – From Research to Business (M4C2), Investment Line 3.1 – Strengthening and creation of Research Infrastructures, Project IR0000034 – “STILES – Strengthening the Italian Leadership in ELT and SKA”, from INAF under the Large GO 2024 funding scheme (project “MeerKAT and Euclid Team up: Exploring the galaxy-halo connection at cosmic noon”), the Large Grant 2022 funding scheme (project “MeerKAT and LOFAR Team up: a Unique Radio Window on Galaxy/AGN co-Evolution”) and the Mini Grant 2023 funding scheme (project ‘Low radio frequencies as a probe of AGN jet feedback at low and high redshift’). M.A.B. is supported by a UKRI Stephen Hawking Fellowship (EP/X04257X/1). LOFAR is the Low Frequency Array designed and constructed by ASTRON. It has observing, data processing, and data storage facilities in several countries, which are owned by various parties (each with their own funding sources), and which are collectively operated by the LOFAR ERIC under a joint scientific policy. The LOFAR resources have benefited from the following recent major funding sources: CNRS-INSU, Observatoire de Paris and Université d’Orléans, France; BMBF, MIWF-NRW, MPG, Germany; Science Foundation Ireland (SFI), Department of Business, Enterprise and Innovation (DBEI), Ireland; NWO, The Netherlands; The Science and Technology Facilities Council, UK; Ministry of Science and Higher Education, Poland; The Istituto Nazionale di Astrofisica (INAF), Italy. This research made use of the Dutch national e-infrastructure with support of the SURF Co-operative (e-infra 180169) and the LOFAR e-infra group. The Jülich LOFAR Long Term Archive and the German LOFAR network are both coordinated and operated by the Jülich Supercomputing Centre (JSC), and computing resources on the supercomputer JUWELS at JSC were provided by the Gauss Centre for Supercomputing e.V. (grant CHTB00) through the John von Neumann Institute for Computing (NIC). This research made use of the University of Hertfordshire high-performance computing facility and the LOFAR-UK computing facility located at the University of Hertfordshire and supported by STFC [ST/P000096/1], and of the Italian LOFAR IT computing infrastructure supported and operated by INAF, and by the Physics Department of Turin university (under an agreement with Consorzio Interuniversitario per la Fisica Spaziale) at the C3S Supercomputing Centre, Italy. This research is part of the project LOFAR Data Valorization (LDV) [project numbers 2020.031, 2022.033, and 2024.047] of the research programme Computing Time on National Computer Facilities using SPIDER that is (co-)funded by the Dutch Research Council (NWO), hosted by SURF through the call for proposals of Computing Time on National Computer Facilities. We thank the staff of the GMRT who made these observations possible. The GMRT is run by the National Centre for Radio Astrophysics (NCRA) of the Tata Institute of Fundamental Research (TIFR). This research made use of the NASA/IPAC Extragalactic Database (NED), which is operated by the Jet Propulsion Laboratory, California Institute of Technology, under contract with the National Aeronautics and Space Administration. Based on observations obtained with *XMM-Newton*, an ESA science mission with instruments and contributions directly funded by ESA Member States and NASA.

Antas, A. S. R., Caproni, A., Machado, R. E. G., Laganá, T. F., & Souza, G. S. 2024, MNRAS, 533, 1341

Bardelli, S., Schinnerer, E., Smolčić, V., et al. 2010, A&A, 511, A1

Beck, R., Ehle, M., Shoutenkov, V., Shukurov, A., & Sokoloff, D. 1999, Nature, 397, 324

Becker, R. H., White, R. L., & Helfand, D. J. 1994, in Astronomical Society of the Pacific Conference Series, Vol. 61, Astronomical Data Analysis Software and Systems III, ed. D. R. Crabtree, R. J. Hanisch, & J. Barnes, 165

Best, P. N., Kauffmann, G., Heckman, T. M., et al. 2005, Monthly Notices of the Royal Astronomical Society, 362, 25

Bîrzan, L., Rafferty, D. A., Nulsen, P. E. J., et al. 2012, MNRAS, 427, 3468

Botteon, A., van Weeren, R. J., Eckert, D., et al. 2024, A&A, 690, A222

Bourne, M. A. & Sijacki, D. 2021, MNRAS, 506, 488

Bourne, M. A., Sijacki, D., & Puchwein, E. 2019, MNRAS, 490, 343

Bourne, M. A. & Yang, H.-Y. K. 2023, Galaxies, 11, 73

Brienza, M., Godfrey, L., & Morganti, R. 2016, in Active Galactic Nuclei: What’s in a Name?, 102

Brienza, M., Godfrey, L., Morganti, R., et al. 2017, A&A, 606, A98

Brienza, M., Lovisari, L., Rajpurohit, K., et al. 2022, A&A, 661, A92

Brienza, M., Rajpurohit, K., Churazov, E., et al. 2025, arXiv e-prints, arXiv:2502.18244

Brienza, M., Shimwell, T. W., de Gasperin, F., et al. 2021, Nature Astronomy, 5, 1261

Buch, K. D., Kale, R., Muley, M., Kudale, S., & Ajithkumar, B. 2023, Journal of Astrophysics and Astronomy, 44, 37

Buch, K. D., Kale, R., Naik, K. D., et al. 2022, Journal of Astronomical Instrumentation, 11, 2250008

Chandra, P. & Kanekar, N. 2017, ApJ, 846, 111

Damsted, S., Finoguenov, A., Lietzen, H., et al. 2024, arXiv e-prints, arXiv:2403.17055

de Gasperin, F., Intema, H. T., Shimwell, T. W., et al. 2017, Science Advances, 3, e1701634

Dunn, R. J. H., Allen, S. W., Taylor, G. B., et al. 2010, Monthly Notices of the Royal Astronomical Society, 404, 180

Eckert, D., Gaspari, M., Gastaldello, F., Le Brun, A. M. C., & O’Sullivan, E. 2021, Universe, 7, 142

Eckert, D., Gastaldello, F., Lovisari, L., et al. 2025, arXiv e-prints, arXiv:2506.13907

Eckert, D., Gastaldello, F., O’Sullivan, E., et al. 2024, Galaxies, 12, 24

Eckert, D., Vazza, F., Ettori, S., et al. 2012, A&A, 541, A57

Eke, V. R., Baugh, C. M., Cole, S., et al. 2004, MNRAS, 348, 866

Ettori, S., Rasia, E., Fabjan, D., Borgani, S., & Dolag, K. 2012, MNRAS, 420, 2058

Fabian, A. C. 2012, ARA&A, 50, 455

Finoguenov, A., Borgani, S., Tornatore, L., & Böhringer, H. 2003, A&A, 398, L35

Forbes, D. A., Ponman, T., Pearce, F., et al. 2006, PASA, 23, 38

Gaspari, M., Eckert, D., Ettori, S., et al. 2019, ApJ, 884, 169

Gaspari, M., Ruszkowski, M., & Oh, S. P. 2013, MNRAS, 432, 3401

Geller, M. J. & Huchra, J. P. 1983, ApJS, 52, 61

Ghirardini, V., Eckert, D., Ettori, S., et al. 2019, A&A, 621, A41

Giacintucci, S., O’Sullivan, E., Vrtilek, J., et al. 2011, ApJ, 732, 95

Giudini, S., Pierini, D., Finoguenov, A., et al. 2009, ApJ, 703, 982

Gozaliasl, G. 2016, PhD thesis, University of Helsinki, Finland

Gozaliasl, G., Finoguenov, A., Babul, A., et al. 2024, A&A, 690, A315

Gozaliasl, G., Finoguenov, A., Khosroshahi, H. G., et al. 2018, MNRAS, 475, 2787

Gozaliasl, G., Finoguenov, A., Khosroshahi, H. G., et al. 2020, A&A, 635, A36

Grogan, N. A. & Geller, M. J. 2000, AJ, 119, 32

Grossová, R., Werner, N., Massaro, F., et al. 2022, ApJS, 258, 30

Haines, C. P., Finoguenov, A., Smith, G. P., et al. 2018, MNRAS, 477, 4931

Hale, C. L., McConnell, D., Thomson, A. J. M., et al. 2021, PASA, 38, e058

Hardcastle, M. J. & Croston, J. H. 2020, New A Rev., 88, 101539

Hlavacek-Larrondo, J., Li, Y., & Churazov, E. 2022, in Handbook of X-ray and Gamma-ray Astrophysics, ed. C. Bambi & A. Sanganello, 5

Hodgson, T., Bartalucci, I., Johnston-Hollitt, M., et al. 2021, ApJ, 909, 198

Jamrozy, M., Konar, C., Machalski, J., & Saikia, D. J. 2008, MNRAS, 385, 1286

Jennings, F. J., Babul, A., Davé, R., Cui, W., & Rennehan, D. 2025, MNRAS, 536, 145

Kale, R. & Ishwara-Chandra, C. H. 2021, Experimental Astronomy, 51, 95

Kale, R., Parekh, V., Rahaman, M., et al. 2022, MNRAS, 514, 5969

Kolokythas, K., O’Sullivan, E., Giacintucci, S., et al. 2015, MNRAS, 450, 1732

Kolokythas, K., O’Sullivan, E., Giacintucci, S., et al. 2020, MNRAS, 496, 1471

Kolokythas, K., O’Sullivan, E., Intema, H., et al. 2019, MNRAS, 489, 2488

Kolokythas, K., O’Sullivan, E., Raychaudhury, S., et al. 2018, MNRAS, 481, 1550

Kolokythas, K., Vaddi, S., O’Sullivan, E., et al. 2022, MNRAS, 510, 4191

Konar, C., Saikia, D. J., Jamrozy, M., & Machalski, J. 2006, MNRAS, 372, 693

Lacy, M., Baum, S. A., Chandler, C. J., et al. 2020, PASP, 132, 035001

## References

Alonso, S., Mesa, V., Padilla, N., & Lambas, D. G. 2012, A&A, 539, A46

Lilly, S. J., Le Brun, V., Maier, C., et al. 2009, The Astrophysical Journal Supplement Series, 184, 218

Lisenfeld, U. & Völk, H. J. 2000, A&A, 354, 423

Liu, W., Sun, M., Nulsen, P., et al. 2019, MNRAS, 484, 3376

Loubser, S. I., Hoekstra, H., Babul, A., & O'Sullivan, E. 2018, Monthly Notices of the Royal Astronomical Society, 477, 335

Lovisari, L., Ettori, S., Gaspari, M., & Giles, P. A. 2021, Universe, 7, 139

Lovisari, L., Reiprich, T. H., & Schellenberger, G. 2015, A&A, 573, A118

Malavasi, N., Bardelli, S., Ciliegi, P., et al. 2015, A&A, 576, A101

McConnell, D., Hale, C. L., Lenc, E., et al. 2020, PASA, 37, e048

McIntosh, D. H., Guo, Y., Hertzberg, J., et al. 2008, MNRAS, 388, 1537

McKean, J. P., Godfrey, L. E. H., Vegetti, S., et al. 2016, MNRAS, 463, 3143

McNamara, B. R. & Nulsen, P. E. J. 2007, ARA&A, 45, 117

Miles, T. A., Raychaudhury, S., Forbes, D. A., et al. 2004, MNRAS, 355, 785

Morganti, R., Frieswijk, W., Oonk, R. J. B., Oosterloo, T., & Tadhunter, C. 2013, A&A, 552, L4

Nelson, D., Pillepich, A., Ayromlou, M., et al. 2024, A&A, 686, A157

Offringa, A. R., de Bruyn, A. G., Zaroubi, S., et al. 2013, A&A, 549, A11

Offringa, A. R., McKinley, B., Hurley-Walker, N., et al. 2014, MNRAS, 444, 606

O'Sullivan, E., Kolokythas, K., Kantharia, N. G., et al. 2018, MNRAS, 473, 5248

O'Sullivan, E., Ponman, T. J., Kolokythas, K., et al. 2017, MNRAS, 472, 1482

O'Sullivan, E., Rajpurohit, K., Schellenberger, G., et al. 2024, ApJ, 970, 65

O'Sullivan, E., Worrall, D. M., Birkshaw, M., et al. 2011, MNRAS, 416, 2916

Panagoulia, E. K., Fabian, A. C., & Sanders, J. S. 2013, Monthly Notices of the Royal Astronomical Society, 438, 2341

Pasini, T., Finoguenov, A., Brüggen, M., et al. 2021, MNRAS, 505, 2628

Pasini, T., Mahatma, V. H., Brienza, M., et al. 2025, A&A, 693, A94

Pearson, W. J., Santos, D. J. D., Goto, T., et al. 2024, A&A, 686, A94

Perley, R. A. & Butler, B. J. 2017, ApJS, 230, 7

Ponman, T. J., Cannon, D. B., & Navarro, J. F. 1999, Nature, 397, 135

Ponman, T. J., Sanderson, A. J. R., & Finoguenov, A. 2003, MNRAS, 343, 331

Rafferty, D. A., McNamara, B. R., Nulsen, P. E. J., & Wise, M. W. 2006, ApJ, 652, 216

Rajpurohit, K., O'Sullivan, E., Schellenberger, G., et al. 2024, arXiv e-prints, arXiv:2408.15197

Randriamanakoto, Z., Ishwara-Chandra, C. H., & Taylor, A. R. 2020, MNRAS, 496, 3381

Riseley, C. J., Vernstrom, T., Lovisari, L., et al. 2025, arXiv e-prints, arXiv:2503.08840

Robotham, A. S. G., Norberg, P., Driver, S. P., et al. 2011, MNRAS, 416, 2640

Rodriguez-Gomez, V., Genel, S., Vogelsberger, M., et al. 2015, MNRAS, 449, 49

Sabater, J., Best, P. N., Hardcastle, M. J., et al. 2019, A&A, 622, A17

Salvetti, D., Marelli, M., Gastaldello, F., et al. 2017, Experimental Astronomy, 44, 309

Scaife, A. M. M. & Heald, G. H. 2012, MNRAS, 423, L30

Schellenberger, G., Vrtilek, J. M., David, L., et al. 2017, ApJ, 845, 84

Shabala, S. S., Ash, S., Alexander, P., & Riley, J. M. 2008, Monthly Notices of the Royal Astronomical Society, 388, 625

Sharma, R. S., Choi, E., Somerville, R. S., et al. 2024, MNRAS, 527, 9461

Shimwell, T. W., Hardcastle, M. J., Tasse, C., et al. 2022, A&A, 659, A1

Shimwell, T. W., Röttgering, H. J. A., Best, P. N., et al. 2017, A&A, 598, A104

Shimwell, T. W., Tasse, C., Hardcastle, M. J., et al. 2019, A&A, 622, A1

Shin, J., Woo, J.-H., & Mulchaey, J. S. 2016, The Astrophysical Journal Supplement Series, 227, 31

Shulevski, A., Brienza, M., Massaro, F., et al. 2024, A&A, 682, A171

Shulevski, A., Morganti, R., Harwood, J. J., et al. 2017, A&A, 600, A65

Solanes, J. M., Perea, J. D., & Valenti-Rojas, G. 2018, A&A, 614, A66

Stewart, G. S. C., Shabala, S. S., Turner, R. J., et al. 2025, PASA, 42, e152

Stott, J. P., Collins, C. A., Sahlén, M., et al. 2010, ApJ, 718, 23

Subrahmanyam, R., Beasley, A. J., Goss, W. M., Golap, K., & Hunstead, R. W. 2003, AJ, 125, 1095

Sun, M. 2012, New Journal of Physics, 14, 045004

Sun, M., Voit, G. M., Donahue, M., et al. 2009, ApJ, 693, 1142

Tasse, C., Shimwell, T., Hardcastle, M. J., et al. 2021, A&A, 648, A1

Taylor, J. E. & Babul, A. 2005, Monthly Notices of the Royal Astronomical Society, 364, 515

Tempel, E., Tuvikene, T., Kipper, R., & Libeskind, N. I. 2017, A&A, 602, A100

Timmerman, R., van Weeren, R. J., Botteon, A., et al. 2022, A&A, 668, A65

van den Bosch, F. C., Jiang, F., Hearin, A., et al. 2014, MNRAS, 445, 1713

van Weeren, R. J., Shimwell, T. W., Botteon, A., et al. 2021, A&A, 651, A115

van Weeren, R. J., Williams, W. L., Hardcastle, M. J., et al. 2016, ApJS, 223, 2

Von Der Linden, A., Best, P. N., Kauffmann, G., & White, S. D. M. 2007, MNRAS, 379, 867

Williams, W. L., van Weeren, R. J., Röttgering, H. J. A., et al. 2016, MNRAS, 460, 2385

Wójtowicz, A., Stawarz, Ł., Cheung, C. C., Werner, N., & Rudka, D. 2023, ApJ, 944, 195

## **Appendix A: Spectral index error maps**

Here we have shown the spectral index error maps corresponding to the Figure 4.

## **Appendix B: Image for the SDSSTG16393**

The X-ray surface brightness map for the full FoV of the group SDSSTG16393.

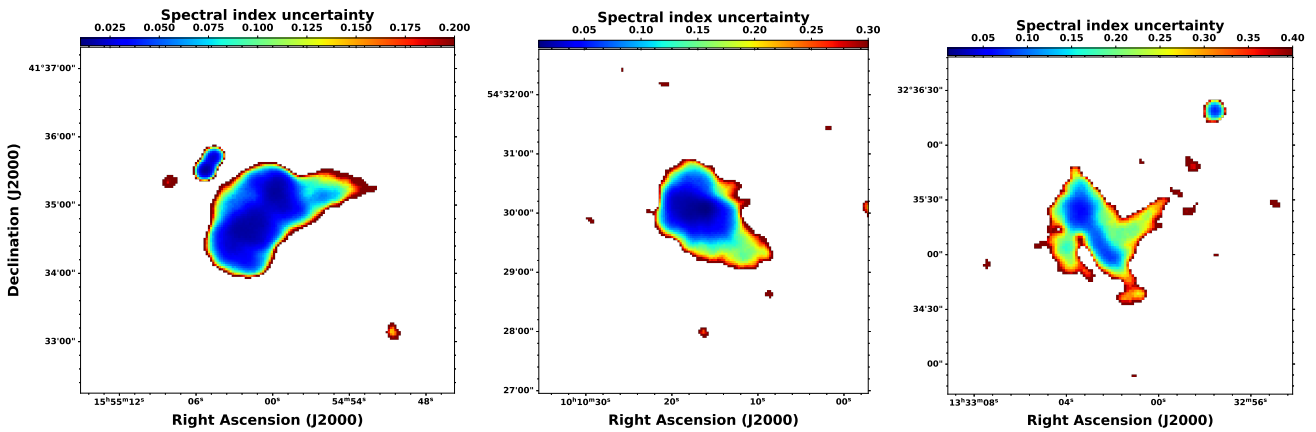


**Fig. A.1.** *Left:* The spectral index error map between 144 and 400 MHz is shown for SDSSTG8102. *middle:* The same is shown for the SDSSTG16393. *Right:* The spectral error map is shown for SDSSTG28674 in a colour scale.

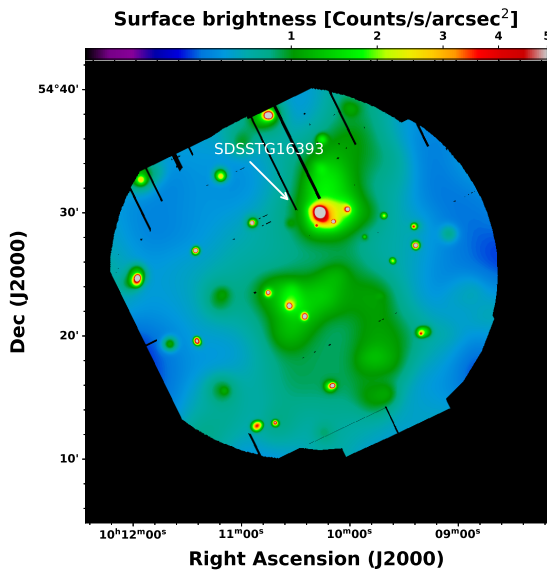


**Fig. B.1.** Adaptively smoothed 0.7 – 1.2 keV image of the full FoV is shown in colour for SDSSTG16393